Polarized reflectivity and lattice dynamics calculation of multiferroic $YMnO_3$

M. Zaghrioui, V. Ta Phuoc, R. A. Souza, and M. Gervais
Laboratoire d'Électrodynamique des Matériaux Avancés, CNRS UMR 6157-CEA, Université F. Rabelais, UFR Sciences, Parc de Grandmont, 37200 Tours, France

(Received 22 May 2008; revised manuscript received 18 August 2008; published 21 November 2008)

Temperature-dependent reflectivity spectra of a multiferroic hexagonal $YMnO_3$ single crystal were measured with polarized light in the ferroelectric phase. The phonon parameters for both $E \| c$ and $E \perp c$ polarizations are obtained by fitting the dielectric function to experimental data. Phonon assignment is done on the basis of lattice dynamics calculations. Phonon anomalies are found at the antiferromagnetic transition T_N. Mean Born effective charges are calculated from phonon fit parameters and discussed in the framework of the different mechanisms proposed for the origin of ferroelectricity in hexagonal multiferroic manganites.

DOI: 10.1103/PhysRevB.78.184305 PACS number(s): 78.30.−j, 63.20.−e, 77.84.Bw

I. INTRODUCTION

Materials combining different ferroic properties have recently attracted a lot of attention because of their puzzling physics and potential novel applications.[1,2] Indeed, in these few systems, both ferroelectric and magnetic orderings are coupled.

Hexagonal manganites $RMnO_3$ (R is a rare earth) belong to this class of materials. When the ionic radius of R is small enough (R=Ho, Er, Tm, Yb, Lu, Y, and Sc), rare-earth manganites $RMnO_3$ crystallize in hexagonal structure with space group $P6_3cm$.[3] These compounds become ferroelectric below 590–1000 K and strongly frustrated antiferromagnets below $\approx$100 K.[4–6]

In the hexagonal phase of $RMnO_3$, each Mn ion is surrounded by three in-plane and two apical oxygen ions forming a MnO_5 trigonal bipyramid (Fig. 1). These MnO_5 blocks are two dimensionally connected with each other on their corners separated by a layer of R^{3+} ions.

Hexagonal $YMnO_3$ is one of the most studied hexagonal manganite. This compound shows a ferroelectric transition at T_C=914 K and antiferromagnetic order below T_N=80 K.[5] The ferroelectric phase is characterized by a buckling of the layered MnO_5 bipyramid, accompanied by off-center displacements of Y and in-plane O_p ions.[7] The magnetic order is determined by the strong in-plane antiferromagnetic superexchange interaction of the Mn^{3+} spins and their geometric frustration.[8,9] The ferroelectric and magnetic order couplings in $YMnO_3$ were evidenced by Huang *et al.*[10] This coupling can result in the so-called magnetoelectric effect with an interesting potential use for devices.[11] Both ferroelectric and antiferromagnetic ground states as well as their coupling are not well understood yet. Van Aken *et al.*,[7] using single-crystal x-ray diffraction and first-principles density-functional calculations, argued that the origin of ferroelectricity in $YMnO_3$ could be driven by electrostatic and size effects. This mechanism is fundamentally different from that usually observed in ferroelectric perovskite oxides such as $BaTiO_3$ and $SrTiO_3$.[12] In these latter compounds, electric polarization is associated to changes in chemical bonding which induces anomalies in Born effective charges on the active ions. By contrast, the Born effective charges calculated for Y, Mn, and O ions are very close to the formal ionic charges, which suggest a new mechanism in this ferroelectric material.[7] However, Cho *et al.*[13] recently proposed that ferroelectricity is most likely driven by Y d^0-ness with rehybridization of Y 4d and O 2p. In such a scenario, a large charge transfer implies large Born effective charge anomalies on Y and O_p atoms at the transition.

Raman scattering and far infrared optical spectroscopies are powerful tools to investigate the driving force of ferroelectricity. Indeed, these methods allow us to track for a possible soft phonon mode driven ferroelectric transition or to extract average Born effective charge through the so-called LO-TO splitting.[12,14,15] Iliev *et al.*[16] reported on Raman scattering on single crystal and infrared transmission on polycrystalline $YMnO_3$ sample at room temperature. The Raman spectra were done in some exact configurations, which permit to determine the symmetry of each observed mode. The infrared active modes were assigned on the basis of lattice dynamics calculations. Also, Kim *et al.*[17] reported nonpolar-

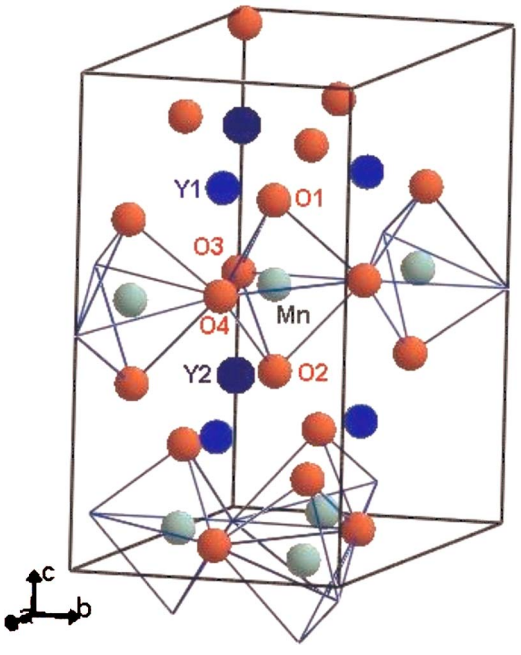

FIG. 1. (Color online) Representation of crystallographic structure of hexagonal $YMnO_3$.

ized Raman and IR reflectance spectra at room temperature on platelike single crystal with the *c* axis perpendicular to the surfaces. However, unambiguous phonon assignment on polycrystalline sample remains a difficult task due to mixing of *ab*-plane and *c*-axis responses.

On the other hand, optical conductivity of $LuMnO_3$ single crystal as function of temperature was reported by Souchkov *et al.*[18] The temperature dependence of some phonon frequencies, in the $E \perp c$ configuration, displays a strong shift at magnetic transition temperature suggesting a spin-phonon coupling in *ab* plane. Moreover, a strongly temperature-dependent electronic excitation centered at 1.7 eV in $E \perp c$ configuration was observed. This transition was attributed to the on-site Mn $d_{x^2-y^2,xy} \rightarrow d_{3z^2-r^2}$ hybridized with O $2p$. In addition, dependence of this transition peak position presents an anomaly at T_N similarly to that observed for some phonon modes in $E \perp c$ configuration. These observations suggest a dominant spin-phonon interaction effect on the in-plane bonds stretching displacements.

In this paper, we report on the first measurements of temperature-dependent polarized reflectivity of hexagonal $YMnO_3$ single crystal for both *ab*-plane and *c*-axis polarizations. Phonon modes are assigned, thanks to lattice dynamics calculation. In-plane phonon anomalies are found at the antiferromagnetic transition, showing a coupling between lattice and magnetic properties. The mean Born effective charges are calculated from fit parameters. The obtained values are discussed in the framework of the different mechanisms proposed for the origin of ferroelectricity in hexagonal $YMnO_3$.

II. EXPERIMENTAL DETAILS

The sample was made in a two-stage process. In the first stage a polycrystalline $YMnO_3$ was prepared by modified citrate method. Citric acid, acrylamid, and N,N-bis was added to appropriate mixture of $Y(NO_3)_3$ and $Mn(NO_3)_2$ solutions to form a gel. The former was decomposed at 650 °C in air, leading to homogeneous and reactive powder. The powder was subsequently annealed at 1000 °C in air. The second crystal-growth stage was carried out by the floating zone technique using a four mirror furnace. Single crystalline rod of about 6 mm in diameter and 45 mm in length was obtained from the growth. The crystallinity of the crystal was checked by Laue x-ray diffraction. The elemental cationic composition was checked using energy dispersive x-ray spectroscopy, and the cation ratio of Y over Mn was close to 1. The Néel temperature was determined by electron spin resonance measurements (T_N=80 K).

Near normal incidence reflectivity spectra were measured as a function of temperature with a BRUKER IFS 66 v/S in the range of 50–18 000 cm^{-1}. The crystal was cut perpendicular to the *b* axis and then polished up to optical grade (0.25 μm) to obtain a mirrorlike surface. The light was polarized both along and perpendicular to the *c* axis. After the initial measurement, the sample was coated *in situ* with a gold film and remeasured as a function of temperature for both polarizations. These additional data were used as reference mirrors to calculate the reflectivity in order to take into account light scattering on the surface of the sample. Lattice dynamics calculations were done using the General Utility Lattice Program (GULP).[19]

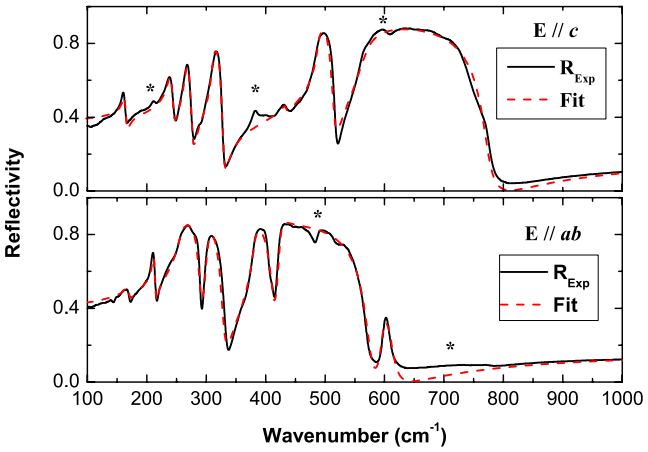

FIG. 2. (Color online) Infrared reflectivity spectra of $YMnO_3$ at 10 K for $E \| c$ and $E \| ab$. The solid line represents the best fits using dielectric function [Eq. (1)].

III. RESULTS AND DISCUSSION

Reflectivity spectra of $YMnO_3$ single crystal for $E \| c$ and $E \perp c$ at 10 K are shown in Fig. 2. The results show a large anisotropy. The small bumps (marked by asterisk in Fig. 2) are due to the imperfect orientation of the crystal and polarization leakage.

In order to investigate in detail phonon properties, reflectivity spectra were fitted with usual Drude-Lorentz oscillators,

$$R(\omega) = \left| \frac{1 - \sqrt{\epsilon(\omega)}}{1 + \sqrt{\epsilon(\omega)}} \right|^2, \tag{1}$$

with

$$\epsilon(\omega) = \epsilon_b^{\infty} + \sum_i \frac{\omega_{p,i}^2}{\omega_{\mathrm{TO},i}^2 - \omega^2 - i\gamma_i\omega}, \tag{2}$$

where ϵ_∞ is the high-frequency dielectric function, $\omega_{p,i}$, $\omega_{\mathrm{TO},i}$, and γ_i are the effective plasma frequency, the transverse frequency, and the damping of the *i*th phonon mode, respectively. Fit parameters for 10 and 300 K are shown in Tables I and II. Twenty-three infrared active phonon modes are predicted by group theory at the Brillouin-zone center of the hexagonal $YMnO_3$ (space group $P6_3cm$). These modes split into 9 A_1 and 14 E_1 modes with the electrical dipole moment aligned along and perpendicularly to the *c* axis, respectively (see Ref. 16 for more details).

Figure 3 presents the optical conductivity in the phonon region at 10 and 300 K with $E \| c$ and $E \perp c$. Note that phonon spectra strongly differ from those reported for the orthorhombic $YMnO_3$.[20]

At room temperature, seven A_1 modes located at 154, 235, 260, 304, 432, 486, and 562 cm^{-1} and eight E_1 modes at 162, 207, 249, 299, 380, 400, 416, and 594 cm^{-1} are de-

TABLE I. Fit of the reflectivity for $E\|c$ at 10 and 300 K. Parameters are in cm^{-1}.

10 K			300 K		
$\omega_{TO,j}$	$\omega_{p,j}$	γ_j	$\omega_{TO,j}$	$\omega_{p,j}$	γ_j
163	132	5.27	154	100	6.66
239	287	7.91	235	283	16.65
266	318	7.33	260	301	15.19
311	380	6.60	304	369	12.61
434	135	6.97	432	129	10.89
489	803	6.95	486	804	11.55
565	1050	27.97	562	1025	28.92
	$\epsilon_\infty=6.46$			$\epsilon_\infty=6.24$	

tected. Although most of the A_1 modes are detected, only eight of the 14 E_1 modes are observed experimentally. Such a discrepancy could be explained by (i) the small intensity or broadening of some modes, which make them undetectable, and (ii) some modes could be nearly degenerated. The phonon assignment is discussed in detail in Sec. III A.

As temperature is decreased, the phonon spectrum remains qualitatively the same. In particular, no new line appears at the magnetic transition T_N and the overall phonon spectral weight remains almost unchanged. This reflects the fact that the symmetry does not change at T_N. However, some E_1 eigenfrequencies show a clear anomaly at T_N, as displayed in Fig. 4. By contrast, no anomalous temperature dependence is detected for A_1 modes. This is in agreement with results obtained on isostructural multiferroic $LuMnO_3$.[18] Moreover, these results are consistent with the giant magnetoelastic coupling recently found in $YMnO_3$.[21] More precisely, coupling between magnetic and structural properties seems to occur within *ab* plane since no anomaly is observed in A_1 phonon spectrum.

A. Phonon modes' assignment

Phonon modes' assignment was done on the basis of lattice dynamics calculations. The calculations are performed

TABLE II. Fit of the reflectivity for $E\perp c$ at 10 and 300 K. Parameters are in cm^{-1}.

10 K			300 K		
$\omega_{TO,j}$	$\omega_{p,j}$	γ_j	$\omega_{TO,j}$	$\omega_{p,j}$	γ_j
167	112	6.22	162	119	6.15
211	232	3.57	207	254	5.24
257	739	13.37	249	727	27.22
301	316	9.24	299	294	14.90
381	564	9.33	380	557	11.33
409	443	87.73	400	452	114.8
423	350	6.38	416	314	11.96
594	117	13.57	594	111	16.17
	$\epsilon_\infty=5.76$			$\epsilon_\infty=5.6$	

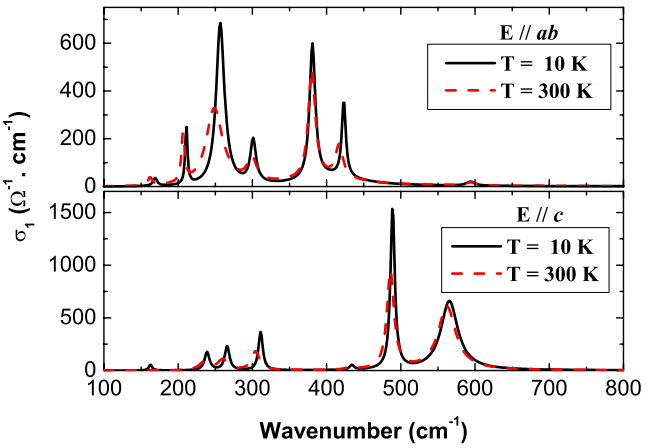

FIG. 3. (Color online) Optical conductivity of $YMnO_3$ single crystal at 10 K (solid line) and 300 K (dashed line) for $E\|c$ and $E\|ab$.

within the framework of the Born-type model. In this approximation, the potentials describing the interatomic interactions between two nonbonded ions, i and j, separated by the distance r_{ij} are presented as follows:

$$U_{ij}=\frac{Z_iZ_je^2}{r_{ij}}+A_{ij}\exp\left(\frac{-r_{ij}}{\rho_{ij}}\right)-\frac{C_{ij}}{r_{ij}^6}, \tag{3}$$

where the first part is the long-range Coulombic term and the latter are the short-range term described by the two-body Buckingham form. Z_i is the effective charge of atom i and A_{ij} (the repulsive parameter), ρ_{ij} (the hardness parameter), and C_{ij} are short-range potential parameters for each pair of atoms obtained by fitting to experimental data. A shell-model treatment of such effect is described in terms of a shell with charge Y connected via an isotropic harmonic spring of force constant k to a massive core of charge Z, namely, $\alpha=Y^2/k$. In the calculations, all ions are treated as polarizable. The calculations were done using GULP.[19] The knowledge of all A_1 modes frequencies and the crystallographic data allows an accurate determination of Buckingham potential parameters.

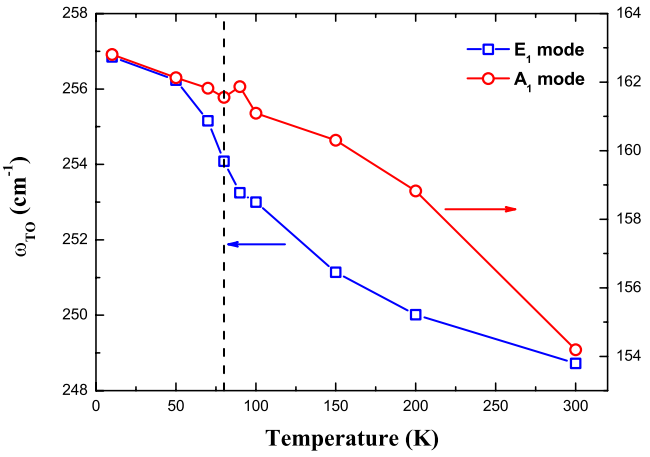

FIG. 4. (Color online) Thermal evolution of transverse optical frequencies for two selected E_1 and A_1 modes.

TABLE III. Short-range potential and shell-model parameters for the hexagonal $YMnO_3$.

	Shell model		
Ion	Z ($\|e\|$)	Y ($\|e\|$)	k (eV Å^{-2})
Mn	1.1	1.9	26
Y	1.4	1.6	20
O	0.86	−2.86	61
	Short-range interaction		
Interaction	A (eV)	ρ (Å)	C (eV Å^6)
Mn-O	2193	0.300	
Y-O	12000	0.250	
O-O	22764	0.149	27.88

Our calculation procedure was as follows: in the first step, the parameters describing the interatomic interactions between two oxygen ions were fixed at the values taken from Lewis library.[22] The rest of parameters was varied to obtain A_1 modes' frequencies, cell parameters, and atomic positions close to experimental values. In the second step, the parameters of O-O interaction were varied to improve the results. The best short-range potential and shell-model parameters are given in Table III. Note that our parameters for Y-O interaction differ from those reported by Iliev *et al.*[16] Indeed, the repulsive parameter (A) is about six times larger than usually reported in literature.[23,24] However, such a small value of this parameter does not lead to obtaining of acceptable values for the modes at low frequencies. On the other hand, the force constant k for both Y and Mn ions is found to be small. These k values indicate a strong polarizability of these ions. Calculated lattice parameters and atomic positions are consistent with experimental values reported in Ref. 26, as shown in Table IV. Comparison between experimental and calculated Raman and infrared phonon frequencies is displayed in Table V. We obtain very good agreement between experimental data and calculations for all the A_1 modes and for nine of the 14 E_1 modes.

According to our modes' assignment, we observe that the phonon modes located at $\omega_{TO}=249$ and 299 cm^{-1}, which present the most marked anomaly at T_N, are related to the displacements of Mn atoms in *ab* plane. This highlights a spin-phonon coupling arising in *ab* plane as observed in $LuMnO_3$.[18] Moreover, this is in agreement with the in-plane antiferromagnetic order and the gigantic magnetoelastic coupling found in this material.[21]

Compared to the data reported by Iliev *et al.*[16] and Kim *et al.*[17] on ceramic material and on platelike single crystal, respectively, three additional modes at 154, 162, and 416 cm^{-1} are detected. On the contrary, we do not observe phonon modes at 457 and 511 cm^{-1}, as reported in these works.

Note that our phonon assignment differs from that of Iliev *et al.*[16] Indeed, the authors attributed the phonon modes from Raman scattering in some exact configurations on a microcrystal and infrared measurements on polycrystalline sample.

TABLE IV. Experimental and calculated lattice and atomic parameters of $YMnO_3$. The experimental atomic positions and lattice parameters were taken from Ref. 13.

		Expt. value[a]	Calc. value
a (Å)		6.120	6.092
b (Å)		11.41	11.75
Mn			
6c (x,0,0)	x	0.3330	0.3339
Y1			
4b (1/3,2/3,z)	z	0.2320	0.2358
Y2			
2a (0,0,z)	z	0.2727	0.2623
O1	x	0.3076	0.3114
6c (x,0,z)	z	0.1625	0.1652
O2	x	0.6414	0.6445
6c (x,0,z)	z	0.3360	0.3296
O3			
2a (0,0,z)	z	0.4757	0.4714
O4			
4b (1/3,2/3,z)	z	0.0163	0.0191

[a]Reference 26.

However, infrared phonon assignment from data on polycrystal remains a difficult task due to mixing of *ab*-plane and *c*-axis responses. Thus, polarized reflectivity on a single crystal allows us to accurately assign all the observed modes and extract quantitative parameters.

B. Effective charges

The Born effective charges Z_k^* quantify the macroscopic electric response of a crystal to internal displacements of its atoms. In principle, the Born effective charges can be calculated from phonon fit parameters since they are directly related to effective plasma frequencies $\omega_{p,i}$ by[14,15]

$$\sum_k \frac{Z_k^{*2}}{m_k} = \frac{v_c}{4\pi}\sum_i \omega_{p,i}^2, \tag{4}$$

where v_c is the unit cell volume, i denotes the phonon mode, and k is the sum over all atoms with the mass m_k and the Born effective charge Z_k^*. Note that Born effective charge involves both static (ionic) and dynamic (electronic) contributions to the dipole moment induced by electric field. The Born effective charge is related to the Scott charge $Z^{(S)}$, which is associated with the ionic contribution to the dipole moment by[25] $Z^*=\epsilon_\infty^{1/2}Z^{(S)}$. Electrical neutrality sum rule provides the additional relation: $\Sigma_k Z_k^*=0$. For binary compounds, this set of equations allows us to determine the mean Born effective charge Z_k^* for each atomic specie. For ternary compounds, the number of unknown parameters exceeds the number of equations. Therefore, Z_k^* cannot usually be determined without additional hypothesis. To overcome this difficulty, one possibility consists of setting the value of the effective charge of one atomic specie (by choosing for example the ionic charge) in order to determine two other

TABLE V. Experimental and calculated frequencies of the A_1 and E_1 phonons and the largest atomic displacements. Raman frequencies are those reported in Ref. 16.

Mode symmetry	Expt. Raman Ref. 16	Expt. IR This work	Expt. IR Calc.	Direction and sign of large atomic displacements
A_1	148	154	140	Y1 $(+z)$, Y2 $(-z)$
A_1	190		161	Y1 $(+z)$
A_1		235	252	Mn $(-z)$, O1, O2, O3, O4 $(+z)$
A_1	257	260	274	Mn $(+x)$, O2 $(-x)$, O3 $(-z)$, O4 $(+z)$
A_1	297	304	325	Mn, O1, O2 $(-x)$, Y2 $(+z)$, O3 $(-z)$
A_1	433	432	434	O1, O2 $(-x)$, O3 $(+z)$, O4 $(-z)$
A_1	490	486	527	Y1, Y2 $(-z)$, O1 $(+x,+z)$, O2 $(-x,+z)$, O3, O4 $(-z)$
A_1		562	554	O1 $(+x)$, O2 $(-x)$, O3, O4 $(+z)$
A_1	681		660	O1 $(+z)$, O2 $(-z)$
E_1			134	Y2 $(+x)$
E_1		162	145	Mn $(+x)$, Y1, Y2 $(-x)$
E_1			157	Y1 $(-y)$, Y2 $(+y)$
E_1		207	198	Y2 $(-x)$
E_1		249	223	Mn $(-x,-y)$
E_1		299	277	Mn, Y1, Y2 $(+x)$, O1, O2 $(-x)$
E_1	376	380	378	Mn $(+x)$, O1 $(+x,+z)$, O2 $(+x,-z)$, O4 $(-x)$
E_1		400	387	O1, O2 $(-y)$, O3, O4 $(+x,+y)$
E_1	408	416	429	O1 $(+x,-z)$, O2 $(+z)$, O4 $(-y)$
E_1			460	O1 $(-x)$, O2 $(+x)$
E_1			471	O1 $(+x)$, O2 $(-x)$
E_1			512	O1 $(-y)$, O3 $(+y)$, O4 $(-x)$
E_1		594	553	O1, O2, O4 $(-x)$, O3 $(+x)$
E_1	632		623	O3 $(-y)$, O4 $(+x)$

Z_k^*'s. Moreover, note that the optical conductivity sum rule states that

$$\frac{120}{\pi}\int_0^{\omega_c}\sigma(\omega)d\omega = \sum_i \omega_{p,i}^2, \tag{5}$$

where ω_c is a cut-off frequency chosen to capture all the phonons spectral weight. Thus, the Born effective charge can also be determined from the real part of the optical conductivity obtained by Kramers-Kronig analysis.

In our case, the unit cell contains 18 O atoms for six Mn and six Y atoms. In addition, O atoms are lighter than Mn and Y atoms. Thus, the contribution of O ions on the right-hand side of Eq. (2) is larger than the contributions of Y or Mn ions. This implies that the value of Z_O^* calculated from our fit parameters is relatively insensitive to the chosen value for either Y atom or Mn atom. Indeed, by varying the value of the effective charge of Y or Mn from $0e$ up to $9e$, which corresponds to three times the ionic charge, the value of Z_O^* changes by only 6%. Thus, Z_O^* is determined with a reasonably good accuracy.

No similar conclusion can be drawn for Z_{Mn}^* and Z_Y^*. To get around this problem and to avoid suspicious assumption on the choice of either Z_{Mn}^* or Z_Y^*, we choose to set $Z_{Mn}^* = Z_Y^*$ as a complementary equation since Mn and Y ions have the same nominal ionic charge. This implies that Z_{Mn}^* and Z_Y^* cannot be determined separately but allows us to evaluate to the mean effective charge of Y and Mn ions. So obtained values for $E\|c$ and $E\perp c$ are summarized in Table VI. The results are compared to the effective charges calculated from optical conductivity reported in Ref. 18 for the isostructural and multiferroic $LuMnO_3$.

The effective charges are quite similar for both $YMnO_3$ and $LuMnO_3$ and clearly deviate from their nominal ionic values (+3 for Y/Lu and Mn and −2 for O). However, the Born effective charges of O do not follow the general trends of other ferroelectric perovskites as $BaZrO_3$, $SrTiO_3$, $CaTiO_3$, $BaTiO_3$, $PbTiO_3$, $CaMnO_3$, or WO_3.[27–29] Indeed, in these ferroelectric oxides, the Born effective charge are expected to be as large as +7.25 for Ti, W, Mn, or Zr atoms and

TABLE VI. Mean Born effective charges deduced from optical conductivity at 300 K for $YMnO_3$ and $LuMnO_3$.

		Z^* (Mn, Y, or Lu)	Z^* (O)
$E\|ab$	$LuMnO_3$	3.8	−2.5
	$YMnO_3$	3.7	−2.5
$E\|c$	$LuMnO_3$	4.3	−2.9
	$YMnO_3$	4.7	−3.1

up to −5.71 for O atoms. This suggests that the mechanism at the origin of ferroelectric properties is different from that occurring in such materials. No obvious temperature dependence is observed between 10 and 300 K. In particular, no change is observed at T_N. On the other hand, the effective charges are found to be very anisotropic. Indeed, the values of Z_k^* for $E\|c$, i.e., parallel to the ferroelectric polarization axis, are larger than for $E\perp c$. These results seem to indicate that the interactions between Mn $3d$/Y $4d$ and O $2p$ atomic orbitals are largely in ionic character. Note that although Z_{Y}^* and Z_{Mn}^* cannot be obtained separately, their mean value is clearly larger than predicted by Van Aken *et al.*[7] from first-principles calculations ($Z_{\mathrm{Y}}^*=3.6$, $Z_{\mathrm{Mn}}^*=3.3$, $Z_{\mathrm{O}_T}^*=-2.3$, and $Z_{\mathrm{O}_P}^*=-2.2$). Such large effective charges are more likely in agreement with the x-ray-absorption spectroscopy (XAS) results of Cho *et al.*[13] Indeed, the authors estimated Y and O_p Born effective charges to be $\approx+8e$ and $\approx-5e$, respectively, in the ferroelectric phase. Thus, our results could provide a support for a scenario of ferroelectricity driven by rehybridization of Y $4d$ and O $2p$. Note also that greater Born effective charges for $E\|c$ than for $E\perp c$ indicate a greater contribution to the ferroelectric polarization. This is in agreement with the vertical shift of the Y ions.[7,21]

IV. CONCLUSION

Phonon dynamics was explored from temperature-dependent reflectivity spectra along both c axis and ab face of a hexagonal $YMnO_3$ single crystal. Almost all of the nine A_1 modes along c axis and 14 E_1 modes in ab plane predicted by the factor group analysis are observed. ab-plane phonon mode frequencies show anomalies at the magnetic transition temperature T_N. In particular, this result is compatible with the gigantic magnetoelastic coupling found in this compound. On the basis of lattice dynamics calculation, phonons modes were assigned for both ab-plane and c-axis directions. Moreover, the fit parameters allow us to calculate the mean Born effective charges. Although Born effective charges cannot be determined separately for each atomic specie, Y and Mn Born effective charges are unambiguously found to be larger than the nominal valences. Such effective charge anomalies provide a support to a mechanism where ferroelectric transition is driven by Y d^0-ness with rehybridization of Y $4d$ and O $2p$.

ACKNOWLEDGMENTS

The authors thank F. Gervais for helpful discussions and critical reading of the paper.

[1] Y. Tokura, J. Magn. Magn. Mater. **310**, 1145 (2007).
[2] N. A. Spaldin and M. Fiebig, Science **309**, 391 (2005).
[3] H. L. Yakel, W. C. Koehler, E. F. Bertaut, and E. F. Forrant, Acta Crystallogr. **16**, 957 (1963).
[4] A. Munoz, J. A. Alonso, M. J. Martinez-Lope, M. T. Casais, J. L. Martinez, and M. T. Fernandez-Diaz, Phys. Rev. B **62**, 9498 (2000).
[5] T. Katsufuji, S. Mori, M. Masaki, Y. Moritomo, N. Yamamoto, and H. Takagi, Phys. Rev. B **64**, 104419 (2001).
[6] J. S. Zhou, J. B. Goodenough, J. M. Gallardo-Amores, E. Moran, M. A. Alario-Franco, and R. Caudillo, Phys. Rev. B **74**, 014422 (2006).
[7] B. Van Aken, T. M. Palstra, A. Filippetti, and N. Spaldin, Nature Mater. **3**, 164 (2004).
[8] P. A. Sharma, J. S. Ahn, N. Hur, S. Park, S. B. Kim, S. Lee, J.-G. Park, S. Guha, and S.-W. Cheong, Phys. Rev. Lett. **93**, 177202 (2004).
[9] M. Tachibana, J. Yamazaki, H. Kawaji, and T. Atake, Phys. Rev. B **72**, 064434 (2005).
[10] Z. J. Huang, Y. Cao, Y. Y. Sun, Y. Y. Xue, and C. W. Chu, Phys. Rev. B **56**, 2623 (1997).
[11] H. Kitahata, K. Tadanaga, T. Minami, N. Fujimura, and T. Ito, Appl. Phys. Lett. **75**, 719 (1999).
[12] W. Zhong, R. D. King-Smith, and D. Vanderbilt, Phys. Rev. Lett. **72**, 3618 (1994).
[13] D. Y. Cho, J. Y. Kim, B. G. Park, K. J. Rho, J. H. Park, H. J. Noh, B. J. Kim, S. J. Oh, H. M. Park, J. S. Ahn, H. Ishibashi, S. W. Cheong, J. H. Lee, P. Murugavel, T. W. Noh, A. Tanaka, and T. Jo, Phys. Rev. Lett. **98**, 217601 (2007).
[14] J. F. Scott, Phys. Rev. B **4**, 1360 (1971).
[15] X. Gonze and C. Lee, Phys. Rev. B **55**, 10355 (1997).
[16] M. N. Iliev, H.-G. Lee, V. N. Popov, M. V. Abrashev, A. Hamed, R. L. Meng, and C. W. Chu, Phys. Rev. B **56**, 2488 (1997).
[17] S. H. Kim, S. H. Lee, T. H. Kim, T. Zyung, Y. H. Jeong, and M. S. Jang, Cryst. Res. Technol. **35**, 19 (2000).
[18] A. B. Souchkov, J. R. Simpson, M. Quijada, H. Ishibashi, N. Hur, J. S. Ahn, S. W. Cheong, A. J. Millis, and H. D. Drew, Phys. Rev. Lett. **91**, 027203 (2003).
[19] J. D. Gale, J. Chem. Soc., Faraday Trans. **93**, 629 (1997).
[20] J. Kim, S. Jung, M. S. Park, S. I. Lee, H. D. Drew, H. Cheong, K. H. Kim, and E. J. Choi, Phys. Rev. B **74**, 052406 (2006).
[21] S. Lee, A. Pirogov, M. Kang, K.-H. Jang, M. Yonemura, T. Kamiyama, S.-W. Cheong, F. Gozzo, N. Shin, H. Kimura, Y. Noda, and J.-G. Park, Nature (London) **451**, 805 (2008).
[22] G. V. Lewis and C. R. A. Catlow, J. Phys. C **18**, 1149 (1985).
[23] S. Sumithra, U. V. Waghmare, and A. M. Umarji, Phys. Rev. B **76**, 024307 (2007).
[24] A. B. Belonoshko, G. Gutierrez, R. Ahuja, and B. Johansson, Phys. Rev. B **64**, 184103 (2001).
[25] S. Tajima, T. Ido, S. Ishibashi, T. Itoh, H. Eisaki, Y. Mizuo, T. Arima, H. Takagi, and S. Uchida, Phys. Rev. B **43**, 10496 (1991).
[26] S. Lee, A. Pirogov, J. H. Han, J. G. Park, A. Hoshikawa, and T. Kamiyama, Phys. Rev. B **71**, 180413(R) (2005).
[27] Ph. Ghosez, J.-P. Michenaud, and X. Gonze, Phys. Rev. B **58**, 6224 (1998).
[28] F. Detraux, Ph. Ghosez, and X. Gonze, Phys. Rev. B **56**, 983 (1997).
[29] A. Filippetti and Nicola A. Spaldin, Phys. Rev. B **68**, 045111 (2003).